PCCP

ROYAL SOCIETY OF CHEMISTRY

PAPER

View Article Online
View Journal | View Issue

Cite this: *Phys. Chem. Chem. Phys.*, 2026, **28**, 112

Multicycle *operando* Raman spectroscopy reveals reversible and irreversible transitions in $LiNiO_2$ electrodes

Eva del Campo Ortiz, [a] Alex R. Neale, [b] Manel Sonni, [cd] Luke M. Daniels, [c] Grazyna Z. Zukowska, [a] Matthew J. Rosseinsky, [cd] Marek Marcinek*[a] and Laurence J. Hardwick *[bd]

Received 19th September 2025,
Accepted 30th October 2025

DOI: 10.1039/d5cp03622d

rsc.li/pccp

Operando Raman spectroscopy of the delithiation and lithiation of $LiNiO_2$ positive electrodes is reported over the first three cycles. Optimisation of the *operando* electrochemical Raman cell configuration facilitated the characterisation of composite electrodes across multiple cycles with high relevance for practical Li-ion cell chemistry. Tracking the E_g and A_{1g} Raman modes highlighted localised irreversible changes, particularly correlated to first-cycle inefficiencies in $LiNiO_2$, followed by reversible band shifts and intensity changes upon subsequent cycles. Furthermore, trends in both the band position and intensities were related to the state of lithiation (x(Li) in Li_xNiO_2) and the phase transitions through hexagonal and monoclinic phases (H1, M, H2 and H3).

1. Introduction

The challenge of *operando* spectroscopy is to recreate measurement conditions as close as possible to the actual system of investigation.[1] In the case of *operando* measurements on battery materials, the motivation is to follow the electrochemical reactions under potential regimes similar to those run in practical cells using commercially relevant electrode formulations, over multiple cycles.[1] This will enable more precise understanding on how the charge storage mechanism and degradation processes evolve over time.

Raman spectroscopy is one such technique that can be readily utilised as an *operando* method through access into an electrochemical cell *via* an optical window.[2–6] *Operando* Raman can offer detailed insights about battery components during cycling[7,8] and provides information about crystal structure, phase compositions, and electronic properties by measuring the frequencies of chemical bond vibrations.[9] Many developments have been reported on improving cell design and electrode configuration so that material capacities and properties can be more closely replicated at both low and high current rates.[10,11]

The Li-ion positive electrode material $LiNiO_2$ has received renewed attention due to the requirement for increased material performance in next-generation Li-ion batteries,[12] and the drive to move away from cobalt-containing active materials. $LiNiO_2$ has a theoretical capacity of 275 Ah kg^{-1} based on full delithiation, but suffers from sustained capacity fade due to irreversible first-order structural phase transitions and large volume changes during cycling.[12] Several Raman studies have been reported for $LiNiO_2$; however, detailed structural characterisation and information on the source of the material is not always provided, making comparable analysis challenging when material synthesis plays a crucial role in the resulting electrochemical performance.[13–16]

Herein, *operando* Raman spectroscopic measurements of electrodes based on structurally well-characterised $LiNiO_2$ are reported over three charge/discharge cycles utilising an improved composite electrode Raman cell configuration. Rapid processing, visualisation, and analysis of the large spectral data sets were aided by the use of the open-source tool PRISMA,[17] highlighting key changes to main spectral bands as a function of lithium (de)intercalation and their relation to reversible and irreversible structural changes during the first cycles.

2. Experimental section

2.1. Synthesis and characterisation of $LiNiO_2$

$LiNiO_2$ was synthesised, as described in our previous study,[18] by ball-milling stoichiometric amounts of dried LiOH and

[a] *Faculty of Chemistry, Warsaw University of Technology, Noakowskiego 3, 00-664 Warsaw, Poland. E-mail: marek.marcinek@pw.edu.pl*
[b] *Stephenson Institute for Renewable Energy, Department of Chemistry, University of Liverpool, Liverpool L69 7ZD, UK. E-mail: hardwick@liverpool.ac.uk*
[c] *Materials Innovation Factory, Department of Chemistry, University of Liverpool, Liverpool L69 7ZD, UK*
[d] *The Faraday Institution, Quad One, Harwell Science and Innovation Campus, Didcot OX11 0RA, UK*

$Ni(OH)_2$ in 45 mL sealed zirconia jars (using seven 10-mm-diameter zirconia balls). Ball milling was performed at 350 rpm for 150 minutes (10 minutes milling, 15 minutes rest) under an argon atmosphere (Fritsch Pulverisette 7 premium line Planetary Ball Mill). The powders were then placed in an alumina crucible inside a quartz tube, which was sealed at both ends using Swagelok end caps. The final black powders were obtained by annealing the ball-milled mixtures at 700 °C for 20 h under flowing dry O_2 gas with a flow rate of 100 mL min^{-1}. The powder was then handled inside an argon-filled glovebox (O_2 < 0.1 ppm, H_2O < 0.1 ppm).

Solutions, measured by inductively coupled plasma mass spectrometry (ICP-MS) in triplicate, were prepared by dissolving 10 mg of powder into 2 mL of concentrated HCl inside an autoclave heated to 100 °C for 12 hours before diluting to 50 mL with ultra-pure water. Measurements were collected on a PerkinElmer ICP-MS NexION 2000 instrument (Table S1).

2.2. Magnetic measurements

Powders of $LiNiO_2$ were pressed into a pellet. A portion of *ca.* 2 mg was loaded into a custom-made quartz tube and sealed under high vacuum ($\sim 2 \times 10^{-5}$ Torr). Magnetisation measurements were carried out using a commercial superconducting quantum interference device magnetometer MPMS3 (Quantum Design, USA). The contribution of the quartz tube to the magnetization was confirmed to be negligible prior to measuring the samples. Zero-field-cooled (ZFC) and field-cooled (FC) measurements at 100 Oe and a subsequent field-cooled measurement at 45 kOe were performed from 2 to 300 K.

A freezing temperature (T_f) of 14 K was determined from the maxima of the 100 Oe zero-field-cooled (ZFC) data for $LiNiO_2$ (Fig. S1a) and the inverse susceptibility of the 45 kOe data show linear Curie–Weiss behaviour (Fig. S1b). Both these observations confirm a near-stoichiometric sample of $LiNiO_2$ is obtained.[12,19,20] The extracted effective moment of 1.731(2) μ_B agrees perfectly with the $S = \frac{1}{2}$ value expected (1.73 μ_B) for Ni^{3+}.

2.3. Structural analysis of $LiNiO_2$

Structural analysis of $LiNiO_2$ was conducted on a ^{7}Li-enriched sample by combining powder X-ray diffraction measured on an X-ray diffractometer (D8 ADVANCE, Bruker) using a Cu-Kα radiation source (λ = 1.5406 Å) and time-of-flight neutron powder diffraction measured at room temperature on the nanoscale-ordered materials diffractometer (NOMAD) at Oak Ridge National Laboratory. The ^{7}Li-enriched samples were synthesised as described above using $^7LiOH{\cdot}H_2O$ (lithium-7-enriched hydroxide monohydrate) dried overnight under dynamic vacuum (<10^{-4} mbar) at 170 °C. Combined Rietveld refinements against SPXRD and NPD data were carried out using Topas (Version 6) software.

2.4. *Operando* Raman spectroscopy cell

The spectroelectrochemical half-cell used for the experiments was the ECC-Opto-Std test cell (EL-Cell), which enables a face-to-face arrangement of the electrodes. The assembly within the Raman cell follows the spacer configuration employed by Rosser *et al.*,[10] including placing a glass fibre (GF) separator above and below the working electrode strip for full electrolyte wetting of the electrode. A small hole (2 mm) was made in the outer separator to allow optical access. The cell was sealed with a Raman-grade CaF_2 window (Crystran), chosen since it only presents a single Raman band at 321 cm^{-1}, which does not interfere with $LiNiO_2$ characteristic bands. The schematic of the cell arrangement is depicted in Fig. S2.

2.5. Electrode preparation

$LiNiO_2$-containing composite electrodes were prepared on 0.05-mm-thick aluminium foil as the current collector. The mass proportions of active material, Super C65 carbon black (CB) and polyvinylidene fluoride (PVDF) binder in the tape-cast composite electrode were 80 : 10 : 10, respectively. These materials were dispersed in *N*-methyl pyrrolidone, and the resulting slurry was centrifugated in Thinky Mixer twice for 10 minutes. Afterwards, the aluminium foil was coated with the slurry using a doctor blade to give a cathode layer with a wet thickness of 150 μm, and this was then dried at 50–60 °C on the heated coating bed. All electrodes were prepared outside the glovebox and further dried for 5 h at 120 °C under vacuum in a Buchi oven. Finally, the electrodes were introduced into an Ar-filled (O_2, H_2O < 1 ppm) glovebox within the oven to avoid contact with air.

Before the final drying step, working electrodes for coin cell and Raman cell measurements were prepared from the tape cast. Regarding coin cells, $LiNiO_2$ electrode discs were cut with a diameter of 12 mm. For the *operando* Raman cell, electrodes were cut in strips of 12 × 3 mm following the optimised studies of Rosser *et al.*[10] The Li metal counter/reference electrode was cut from a ribbon (Sigma-Aldrich, 99%; 0.38 mm thickness) with diameters of 14 mm and 9 mm for coin cells and the Raman cell, respectively. The electrolyte solution used for all the electrochemical measurements was 1 M Li[PF_6] in a 1 : 1 volumetric mixture of ethylene carbonate/dimethyl carbonate (EC : DMC) (Solvionic). Both cell assemblies were carried out within an argon-containing glovebox (O_2, H_2O < 1 ppm). Schematics showing the free-standing and strip-electrode preparation and photographic images of the three types of electrodes used are shown in Fig. S3 and S4, respectively.

2.6. Electrochemical characterisation

Galvanostatic charge–discharge tests within the Raman and coin cells were performed using Biologic VMP-150 potentiostat. The potentials were applied *vs.* the Li-metal counter/reference electrode from 3.0 to 4.3 V *vs.* Li^+/Li to observe the full structural variation.[21] The cell rested for 10 minutes at OCP (*ca.* 3 V) and then 3 cycles were recorded at a C/10 rate (where 1C was defined as 200 mAh g^{-1} herein, based on the approximate practical discharge capacity of $LiNiO_2$). The measurements were completed at room temperature (*ca.* 23 °C) for the *operando* Raman measurements, while the coin cell electrochemical measurements were conducted inside a climate chamber held at 30 °C.

2.7. Raman characterisation

An InVia Renishaw Raman spectrometer was used for the measurement of $LiNiO_2$ tape-cast electrodes situated within the *operando* cell. A 633 nm wavelength laser was focussed through a microscope (Leica) *via* a 50× objective (Leica) onto the electrode with a spatial resolution at the surface of *ca.* 2–3 μm^2 and with a power of 4 mW, which corresponded to a 50% energy attenuation. All Raman measurements for every experiment were performed in a single spot, therefore 3 × 25 s acquisitions per spectrum were selected to avoid sample burning. Consequently, each scan lasted 6 minutes and we therefore obtained around 100 spectra per cycle.

During the *operando* experiments, the optical focus of the microscope on the sample was periodically checked and refocused, if needed, to compensate for minor shifts in focus within the cell during cycling.

2.8. PRISMA data treatment

Before processing the spectral data using PRISMA, the electrochemical and spectroscopic datasets were correlated according to collection times. Once the cycling of the cell had finished, a series of Raman spectra were obtained containing information corresponding to the specific times at which each spectrum was recorded. In parallel, for the electrochemical technique used, the relationship between time and all the independent variables, such as potential, capacity, state of lithiation (x(Li) in Li_xNiO_2) and current, among others, was also logged. Using this information, each spectrum was then correlated to a specific variable before data treatment on PRISMA.[17]

3. Results and discussion

Free-standing electrodes with optical access by a pinhole in the current collector generally deliver expected electrochemical performance at low current rates when graphite is used as the active material.[8,22–24] However, for positive electrode materials such as $LiNiO_2$, analogous methodologies for preparing the free-standing electrode configuration is unsuitable and the observed capacities approach only half the expected capacity values (Fig. 1(a)).

The performance loss in the bespoke free-standing $LiNiO_2$ electrodes severely limits the practical relevance of any correlative *in situ*/*operando* spectroelectrochemical measurements and, instead, direct measurement of composite electrodes more representative of true cell conditions should be targeted. Following the approach by Rosser *et al.*,[10] a rectangular electrode (12 × 3 mm), designated as an electrode strip, was punched from a conventional tape-cast composite electrode containing $LiNiO_2$, conductive carbon black, and polyvinylidene fluoride (Kynar flex) binder. A glass-fibre separator was placed in between the electrode strip and lithium metal with an additional separator, containing a small hole for optical access, located between the window and the working electrode to allow facile electrolyte access (Fig. S2). Compared to the free-standing electrode, the electrochemical performance of the electrode strip is much improved (Fig. 1(b)), approaching the performance of the same composite $LiNiO_2$ electrode material measured within a coin cell (Fig. 1(c)).

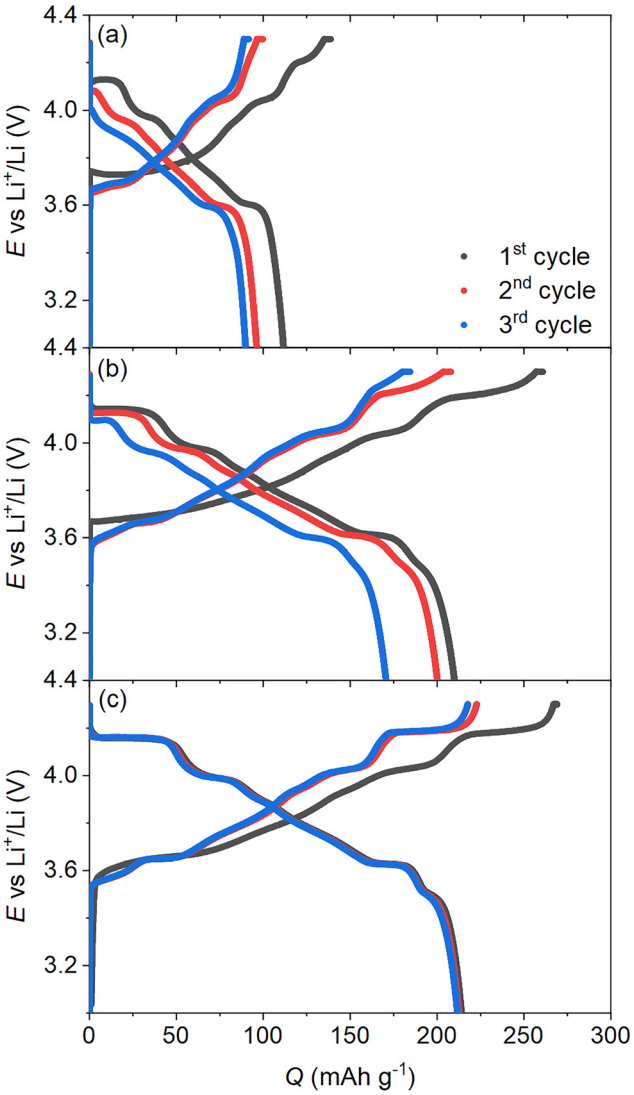

Fig. 1 Potential profiles of the initial three cycles of $LiNiO_2$ *vs.* Li^+/Li in the following configurations: (a) free-standing electrode in the *operando* Raman cell, (b) tape-cast electrode strip (12 × 3 mm) in the *operando* Raman cell assembled as in Fig. S2, and (c) tape-cast electrode disc (Ø = 12 mm) in a coin cell configuration. All cells were cycled between 3–4.3 V *vs.* Li^+/Li at a C/10 rate, based on the mass of $LiNiO_2$ with 1 M $Li[PF_6]$ in ethylene carbonate/dimethyl carbonate (EC : DMC) (1 : 1 vol) electrolyte. Note Raman cell data was collected at 23 °C, whilst coin cell data was collected at 30 °C.

The $LiNiO_2$ investigated within the optical cell was synthesised *via* the solid-state method reported previously, from LiOH and $Ni(OH)_2$ reagents,[18] and is further described within the SI. This method resulted in a powder sample with a stoichiometric composition of $Li_{1.019(20)}Ni_{1.000(27)}O_2$, measured *via* inductively coupled plasma mass spectrometry (ICP-MS) (Table S1). This exact stoichiometry is further supported by assessment of the electronic state of nickel *via* measurement of magnetisation data which accurately confirm the oxidation state of Ni^{3+}

through a measured effective moment of 1.731(2)μ_B (expected value of 1.73μ_B for $S = \frac{1}{2}$) (Fig. S1).

Structural characterisation was performed *via* Rietveld refinement against powder X-ray and neutron diffraction data utilising a multidomain hexagonal $R\bar{3}m$ model reported previously,[25] which accounts for both ordered $R\bar{3}m$ and disordered $Fm\bar{3}m$ domains of differing size that might arise from Li/Ni mixing within the bulk powder (Fig. S5 and Table S2). A chemical order parameter, defined as the difference in Li content between the two distinct cation (Li and Ni) layers (*i.e.*, $\eta = |occ_{Li}–occ_{Ni}|$), of 0.95(3) is extracted from the refinement, indicating a highly ordered structure, with a low degree of cation mixing.

The complete set of *operando* Raman spectra for the first three cycles are shown as stacked plots within Fig. 2(a)–(c), to correlate with the potential/capacity profiles in Fig. 2(d) for cycles 1–3. The data is also displayed as a spectral band intensity heat map in Fig. S6 that visibly shows the changing bands intensity trends as a function of capacity. Two characteristic bands for $LiNiO_2$ are observed at 485 and 545 cm^{-1}, which correspond to the E_g and A_{1g} Raman active modes, respectively.[26,27] The E_g mode is the result of the displacement of oxygen atoms along the oxygen layers, whereas the A_{1g} mode originates from the oxygen displacement parallel to the *c* axis of the structure.[15] The band shape, ratio, and positions of $LiNiO_2$, before cycling, are broadly congruent with spectra reported in previous studies.[13,15,16,27] However, slight variations in the specific band shapes and intensities do arise from the source and quality of the $LiNiO_2$ active material, highlighting the importance of the structural and compositional characterisation of the material reported herein.

During the initial charging step, both the E_g and A_{1g} bands undergo positional shifts and the broad band shapes sharpen as lithium is removed from the structure at increasing potentials. The band sharpening has been attributed to a decrease in the Ni–O bond distance distribution as Li is deintercalated.[16] Additionally, band intensities generally increase as a function of $LiNiO_2$ delithiation as reported previously. Upon first discharge, the spectral bands exhibit partial reversibility in the processes, showing reduced intensity and re-broadening, while the reversibility of the band positions is less clear to the eye. Generally, comparable trends in the band intensity and width are observed during second and third cycles.

However, to extract quantitative information on band changes during cycling and better understand the reversibility of these mechanisms, accurate spectral fitting of the data is critical to obtain specific band positions and intensities as a function of the cell cycling. To achieve this, approximately 100 Raman spectra per cycle (300 total spectra) were fitted using PRISMA as a high-throughput semi-automated spectra processing application and correlated with the cell capacity (*i.e.*, experimental time for a galvanostatic experiment). As a result, the trends in vibrational modes during charge and discharge can be tracked and thereby correlate the observed changes with respect to the various potential, capacity, and, importantly, the state of lithiation (x(Li) in Li_xNiO_2) properties of the $LiNiO_2$ electrode. The full details for the methodology of spectral fitting are presented in the SI (Fig. S7) and the derived spectral

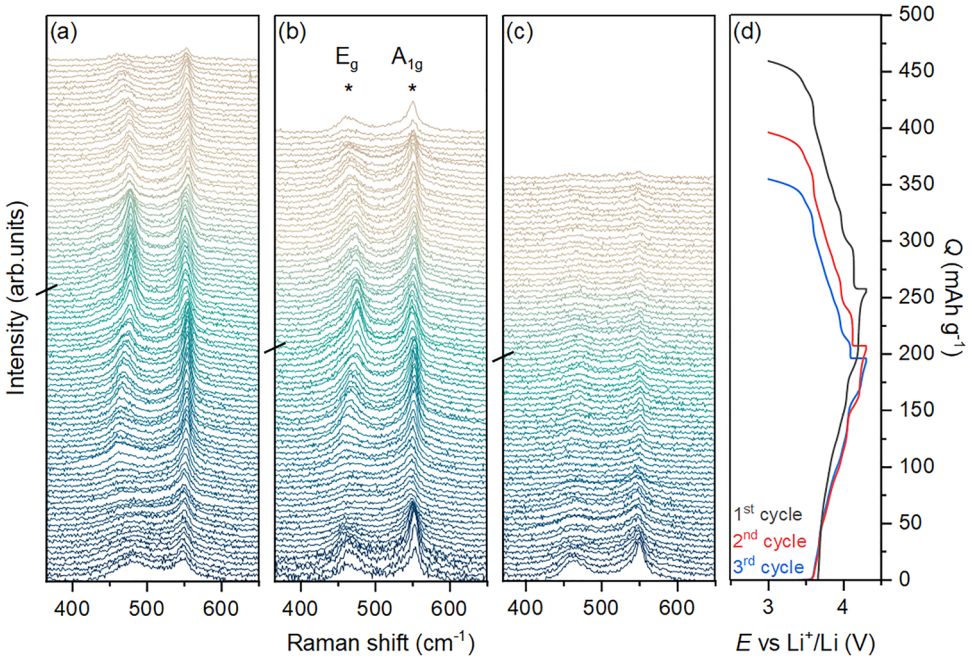

Fig. 2 *Operando* Raman spectra series for (a) cycle 1, (b) cycle 2, and (c) cycle 3 of $LiNiO_2$ tape-cast electrode strip cycled *vs.* Li metal between 3–4.3 V *vs.* Li^+/Li at a C/10 rate with 1 M Li[PF_6] in ethylene carbonate/dimethyl carbonate (EC : DMC) (1 : 1 vol). The stacking between spectra was correlated with the (d) potential profiles of $LiNiO_2$ *vs.* Li^+/Li, represented as cumulative capacity per individual cycle. The two characteristic bands, E_g and A_{1g}, for $LiNiO_2$ were observed at 485 cm^{-1} and 545 cm^{-1}, respectively.[16,27] The breaks on the *y* axis in (a)–(c) represent the end of the charge and the beginning of discharge for each cycle.

information is in good agreement with manual data processing/fitting methods (Fig. S8).

The derived band positions and intensities for the E_g and A_{1g} modes of the $LiNiO_2$ electrode strip during the first three cycles as a function of the cumulative cycling capacity are presented in Fig. 3. The individual band intensities were normalised between 0 to 1 (*i.e.*, $I_{norm}(E_g)$ and $I_{norm}(A_{1g})$). The pre-normalised intensity data for this plot is shown in Fig. S9.

The positions of Raman bands vary with the strength of the interatomic forces within the lattice; therefore, the stronger these forces, the higher the frequencies and, consequently, the higher the wavenumber values.[28,29] Regarding the first-cycle results shown in Fig. 2, trends in the band position shifts matched the *operando* study for $LiNiO_2$ carried out by Jacquet *et al.*,[16] wherein the, E_g and A_{1g} Raman peaks shifted in opposite directions, with both presenting a U-shaped trend during the first half-cycle. However, during this cycle, the band shift range (*ca.* 15 cm^{-1} and 8 cm^{-1} for E_g and A_{1g}, respectively) is more pronounced in this study. Importantly, the cell configuration and electrode design enabled the recording of successive cycles where the measured shift ranges become less pronounced. The E_g mode shifted position between 465–475 cm^{-1} and 461–472 cm^{-1} and the A_{1g} mode shifted between 546–552 cm^{-1} and 544–550 cm^{-1} during the second and third cycles, respectively. The variation in the pattern of the E_g and A_{1g} peak shifts as a function of *x*Li in Li_xNiO_2, observed between cycle 1 and cycles 2/3, suggests a significant local structural change at the surface within the measured potential range that occurs during the first cycle, and is retained on the subsequent cycles.[21]

The data presented in Fig. 3 highlight a key irreversibility in the E_g mode as a function of cycling. Critically, the initial E_g band position in the early stages before charging (*ca.* 480–482 cm^{-1}) is never recovered during the first cycle. Upon delithiation of $LiNiO_2$ to *ca.* $Li_{0.1}NiO_2$ at 4.3 V *vs.* Li^+/Li on the first charge, the U-shape trend is observed, but the band only recovers to *ca.* 475 cm^{-1} and drops to even lower wavenumber values upon re-lithiation (discharge) to 470 cm^{-1} at 3.0 V *vs.* Li^+/Li. Conversely, the observed irreversibility in band position before and after the first cycle is not replicated in subsequent cycles, whereby the observed shifts in the E_g band during the second cycle are broadly replicated within the third cycle. This aligns with the poor first-cycle Coulombic efficiencies of $LiNiO_2$, which improve considerably in the latter two cycles (Fig. 1). Upon initial charging to 4.3 V *vs.* Li^+/Li, $LiNiO_2$ transforms into the H3 structure *via* several intermediate phases, undergoing a substantial 9.4% reduction in unit cell volume, contributing not only to a capacity fade but also to structural disorder.[30] The observed irreversibility in the E_g mode in the Raman spectra likely indicates that the monoclinic structure of $LiNiO_2$ persists locally, even after the first charge to 4.3 V and subsequent lithiation to 3.0 V.[31,32]

To further correlate the observed spectral changes with structural transformations in the material, data was compared with the differential capacity (dQ/dE) response of the electrode (Fig. S12). The dQ/dE response as a function of potential was related to the state of x(Li) in Li_xNiO_2 (Fig. S13), enabling comparison between different phase regions with the changes in Raman bands as a function of the state of lithiation. The Raman band shifts (Fig. S12) and intensities (Fig. S13) are compared with differential capacities as a function of x(Li) in Li_xNiO_2 for the three charging half-cycles.

$LiNiO_2$ presents the electrochemical signatures of the well-established structural phase transformations from the initial hexagonal H1 structure, through monoclinic M, and hexagonal H2 and H3 structures,[33] observed as plateaus in the potential profile and peaks in the dQ/dE plots.[12] The fcc ABCABC stacking sequence of O^{2-} anions in the pristine $R\bar{3}m$ $LiNiO_2$ structure is retained throughout each of these transitions. The H1 phase has been found to persist *via* a solid-solution reaction until $x \approx 0.8$ (*i.e.*, $Li_{0.8}NiO_2$), followed by the M phase until $x = 0.4$–0.36. The H2 phase is the dominant phase down to $x \approx 0.26$, with the H2 to H3 transition occurring between $x = 0.26$–0.16.[33]

The E_g peak positions for the first cycle are depicted in Fig. S13, and the shift towards lower wavenumbers was the result of the softening of the metal–oxygen–metal bonds during delithiation (charging), associated with the hexagonal to monoclinic phase transition beginning from $x < 0.85$ up to the turning point around $x < 0.60$ where the band position begins to rise.[16] The second and third cycles also experienced this event until the turning points of $x < 0.40$ and $x < 0.35$, respectively. The state of lithiation (x(Li) in Li_xNiO_2) ranges for each phase are depicted in Table 1, which, for cycle 1, follows the phase changes described above.[33]

The further phase transitions from monoclinic $LiNiO_2$ to H2 and then H3 are driven by the migration of Ni ions into the lithium layers, which mainly happens during the first cycle.[34] These transitions are correlated with an increase in band position for the E_g mode (Fig. S12) related to the hardening of the metal–oxygen bond as Ni^{3+} is oxidised to Ni^{4+}.[35,36]

Upon re-lithiation, the E_g band did not return to its initial position of 485 cm^{-1}, instead finishing at ~465 cm^{-1} which

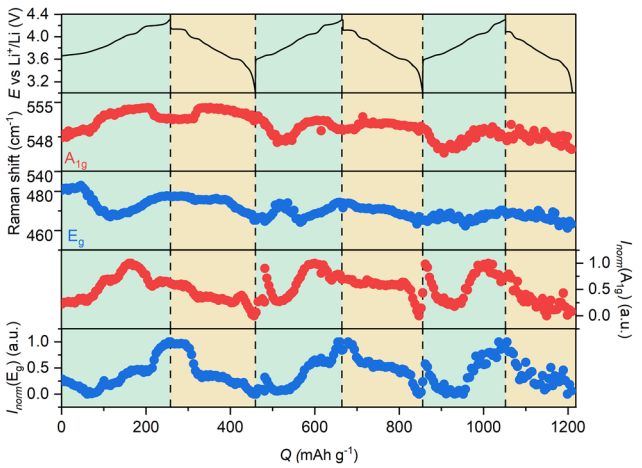

Fig. 3 Potential profiles of $LiNiO_2$ *vs.* Li^+/Li (top), the fitted band positions (middle), and intensities (bottom) extracted from the *operando* Raman spectra and processed by PRISMA. Band intensities were normalised individually per cycle between 0 and 1.

Table 1 x(Li) in Li_xNiO_2 during the first, second and third delithiation (charge) periods with respect to the structural phase transformations extracted from the Raman cell electrochemical data in Fig. 1b

Structure	Potential range/V *vs.* Li^+/Li	x(Li) in Li_xNiO_2		
		1st cycle	2nd cycle	3rd cycle
H1	3–3.65	1–0.85	0.8–0.75	0.75–0.65
H1 + M	3.65–3.73	0.85–0.80	0.75–0.65	0.65–0.55
M	3.73–4.02	0.80–0.45	0.65–0.35	0.55–0.25
M + H2	4.02–4.08	0.45–0.35	0.35–0.25	0.25–0.15
H2	4.08–4.18	0.35–0.25	0.25–0.20	0.15–0.1
H2 + H3	4.18–4.25	0.25–0.1	0.2–0.1	0.1–0.05
H3	>4.25	0.1–0	0.1–0	0.05–0

indicates that $LiNiO_2$ did not return to its original structure (Fig. 3).[37,38] This suggests that Raman spectroscopy is sensitive to local structural irreversibility, highlighting that the bonding within $LiNiO_2$ does not fully revert locally to the initial structure after cycle 1. Despite full discharge to 3 V *vs.* Li^+/Li, the stoichiometry of only *ca.* $Li_{0.8}NiO_2$ is recovered, corresponding approximately with the range of the monoclinic phase (Fig. S11) wherein the terminal E_g band position aligns reasonably well with this position (x = 0.8 for Li_xNiO_2) during charging (Fig. S6). Overall, Raman spectroscopy appears to be more sensitive to these local changes than X-ray powder diffraction, whereby after the 1st cycle, the H1 structure remains the only phase detected.[18] Previously, *ex situ* synchrotron X-ray powder diffraction of $LiNiO_2$ (with low Li/Ni intermixing) revealed that, after 50 charge–discharge cycles, the reflections corresponding to the monoclinic phase began to persist in the diffraction pattern of x = 0 ($LiNiO_2$), indicating that the M–H1 phase transition is not fully reversible upon discharge.[18]

In the second and third cycles, the E_g mode shift values for H3 after charging (*ca.* 470–474 cm^{-1}) are greater than those for the H1 phase (*ca.* 465 cm^{-1}, Fig. S12). The shifting of the A_{1g} peak position to lower Raman shift values (from *ca.* 552 cm^{-1} [cycle 2] and 550 cm^{-1} [cycle 3] to *ca.* 548 and 546 cm^{-1} for cycles 2 and 3, respectively) indicates the elongation of the Ni–O bond along the *c*-axis and a reduction in the intensity of both active modes, which is consistent with the experimental data from the second and third cycles (Fig. S12 and S13).

In general, the discharge (lithiation) trends for the E_g and A_{1g} active modes (Fig. 3) differed from the trends observed during charging, indicating that the phase transitions are not completely reversible for $LiNiO_2$ during discharge for the potential range chosen, as expected, especially for the first cycle.

The data extracted on band intensities for both modes across the first three charge cycles are presented in Fig. 3 and Fig. S13. Band intensity in Raman spectroscopy is related to several parameters, and the general increase in band intensity as a function of lithiation (charging) is rationalised in depth for one cycle by Jacquet *et al.*[16] Overall, the spectral intensity increased during charge and decreased during discharge reversibly for both active modes during all 3 cycles in our study.

The relative intensity ratio ($I(E_g)/I(A_{1g})$) was 1 : 1 at (x(Li) in Li_xNiO_2 = 1) during the first delithiation (Fig. S14). Throughout the initial stages of delithiation, the E_g mode decreased in intensity, while the A_{1g} mode intensity increased during the H1 → M transition. For cycles 2 and 3, and in agreement with the Raman shift results, both intensities decreased until arriving in the monoclinic structure region. During the presence of the M phase, the E_g and A_{1g} intensities increased for all three cycles until reaching the H2 phase, where the A_{1g} intensity experienced a maximum before decreasing at the end of the delithiation.

For the H2 phase, the relative intensity ratio ($I(E_g)/I(A_{1g})$) consistently remained 1 : 2 for the first, second and third cycles at x(Li) in Li_xNiO_2 = 0.35, 0.25 and 0.15, respectively (corresponding to E *vs.* Li^+/Li = 4.08, 4.11, and 4.15 V, respectively, Fig. S14). Across all cycles, the E_g intensity remains constant while the A_{1g} intensity reduces for the H2 phase. Subsequently, at higher potentials, the intensity ratio reverses towards a maximum of $I(E_g)/I(A_{1g}) > 1.2$, associated with the H3 phase transition causing a final increase in E_g intensity. Similar trends were observed in all three charge profiles in Fig. S13, highlighting that changes in band intensities were generally reversible during further cycles for $LiNiO_2$.

4. Conclusions

$LiNiO_2$, with low Li/Ni intermixing, was analysed using *operando* Raman spectroscopy, revealing $LiNiO_2$ structural evolution during the initial three cycles. By using an optimised Raman cell configuration, *operando* electrochemical Raman spectra could be collected for a conventional tape-cast composite electrode with practically representative electrochemical performance for more than one cycle. The fast deconvolution of many spectra across multiple cycles using PRISMA enabled a detailed analysis of the key E_g and A_{1g} modes of $LiNiO_2$. Trends in both the band position and intensities were related to the state of lithiation (x(Li) in Li_xNiO_2) and the phase transitions through hexagonal and monoclinic phases (H1, M, H2 and H3). Tracking of the two key Raman modes (E_g and A_{1g}) across multiple cycles highlighted the sensitivity of the method to irreversible local structural changes, particularly correlated to first cycle inefficiencies in $LiNiO_2$ that account for capacity fade and structural irreversibility, whereby $LiNiO_2$ does not revert to the initial spectra. Subsequent cycle analyses showed greater reversibility in the Raman shifts and intensity variations, highlighting that localised irreversible structural transitions occur predominantly during the first charge of $LiNiO_2$ to 4.3 V *vs.* Li^+/Li.

Author contributions

E. C. O. performed the experiments and analyzed the data. A. R. N. supported the methodology development and data analysis. M. S. and L. D. conducted the PXRD measurements and contributed to data processing. L. J. H. and M. M. provided supervision, resources, and project administration. All authors discussed the results and contributed to writing – review and editing.

Conflicts of interest

There are no conflicts to declare.

Data availability

The data supporting this article have been included as part of the supplementary information (SI). Supplementary information: schematic representation of the *operando* Raman cell configuration, $LiNiO_2$ characterisation data (ICP-MS, magnetic susceptibility, powder XRD and refinements and the derived atomic coordinates and isotropic displacement parameters), supplementary *operando* Raman intensity plots, peak deconvolution information, non-normalised band intensity data trends, differential capacity data, and signal intensity ratio data. See DOI: https://doi.org/10.1039/d5cp03622d.

Acknowledgements

As a part of the DESTINY PhD program, this publication acknowledges funding from the European Union's Horizon 2020 research and innovation program under the Marie Skłodowska-Curie Actions COFUND (Grant Agreement No. 945357). LJH, MJR, and MS acknowledge the financial support from the Faraday Institution CATMAT (EP/S003053/1, FIRG016) and ARN acknowledges funding from the European Union's Horizon 2020 research and innovation programme under grant agreement no 957189 (BIG-MAP). The project is part of BATTERY 2030+, the large-scale European research initiative for inventing the sustainable batteries of the future. Authors acknowledge the support and guidance from Dr Eibar Flores, SINTEF, Norway, on the use of PRISMA.

References

1 L. Meyer, N. Saqib and J. Porter, *J. Electrochem. Soc.*, 2021, **168**, 090561.
2 T. Lenk and U. Schröder, *J. Solid State Electrochem.*, 2024, **28**, 965–979.
3 R. Baddour-Hadjean and J. P. Pereira-Ramos, *AIP Conf. Proc.*, 2010, **1267**, 1137–1138.
4 P. Novák, D. Goers, L. Hardwick, M. Holzapfel, W. Scheifele, J. Ufheil and A. Würsig, *J. Power Sources*, 2005, **146**, 15–20.
5 L. J. Hardwick, M. Hahn, P. Ruch, M. Holzapfel, W. Scheifele, H. Buqa, F. Krumeich, P. Novák and R. Kötz, *Electrochim. Acta*, 2006, **52**, 675–680.
6 J. C. Panitz, F. Joho and P. Novák, *Appl. Spectrosc.*, 1999, **53**, 1188–1199.
7 T. J. Leckie, S. D. Robertson and E. Brightman, *Energy Adv.*, 2024, **3**, 2479–2502.
8 A. R. Neale, D. C. Milan, F. Braga, I. V. Sazanovich and L. J. Hardwick, *ACS Energy Lett.*, 2022, **7**, 2611–2618.
9 R. E. Ruther, A. F. Callender, H. Zhou, S. K. Martha and J. Nanda, *J. Electrochem. Soc.*, 2015, **162**, A98–A102.
10 T. E. Rosser, E. J. F. Dickinson, R. Raccichini, K. Hunter, A. D. Searle, C. M. Kavanagh, P. J. Curran, G. Hinds, J. Park and A. J. Wain, *J. Electrochem. Soc.*, 2021, **168**, 070541.
11 J. S. Weaving, A. Lim, J. Millichamp, T. P. Neville, D. Ledwoch, E. Kendrick, P. F. McMillan, P. R. Shearing, C. A. Howard and D. J. L. Brett, *ACS Appl. Energy Mater.*, 2020, **3**, 7474–7484.
12 M. Bianchini, M. Roca-Ayats, P. Hartmann, T. Brezesinski and J. Janek, *Angew. Chem., Int. Ed.*, 2019, **58**, 10434–10458.
13 C. Lee, Y. Yokoyama, Y. Kondo, Y. Miyahara, T. Abe and K. Miyazaki, *ACS Appl. Mater. Interfaces*, 2020, **12**, 56076–56085.
14 E. Flores, N. Vonrüti, P. Novák, U. Aschauer and E. J. Berg, *Chem. Mater.*, 2018, **30**, 4694–4703.
15 E. Flores, P. Novák and E. J. Berg, *Front. Energy Res.*, 2018, **6**, 1–16.
16 Q. Jacquet, N. Mozhzhukhina, P. N. O. Gillespie, G. Wittmann, L. Perez, F. G. Capone, J. Rueff, S. Belin, R. Dedryvère, L. Stievano, A. Matic, E. Suard, N. B. Brookes, A. Longo, D. Prezzi, S. Lyonnard and A. Iadecola, *Adv. Energy Mater.*, 2024, **14**, 2401413.
17 E. Flores, N. Mozhzhukhina, X. Li, P. Norby, A. Matic and T. Vegge, *Chem. Res.*, 2022, **2**, 1–9.
18 J. Lim, M. Sonni, L. M. Daniels, M. Bahri, M. Zanella, R. Chen, Z. Li, A. R. Neale, H. Niu, N. D. Browning, M. S. Dyer, J. B. Claridge, L. J. Hardwick and M. J. Rossiensky, *Adv. Mater.*, 2025, **37**, 2417899.
19 A. Rougier, P. Gravereau and C. Delmas, *J. Electrochem. Soc.*, 1996, **143**, 1168–1175.
20 D. Goonetilleke, B. Schwarz, H. Li, F. Fauth, E. Suard, S. Mangold, S. Indris, T. Brezesinski, M. Bianchini and D. Weber, *J. Mater. Chem. A*, 2023, **11**, 13468–13482.
21 C. S. Yoon, D. W. Jun, S. T. Myung and Y. K. Sun, *ACS Energy Lett.*, 2017, **2**, 1150–1155.
22 C. Sole, N. E. Drewett and L. J. Hardwick, *Faraday Discuss.*, 2014, **172**, 223–237.
23 J. Zou, C. Sole, N. E. Drewett, M. Velický and L. J. Hardwick, *J. Phys. Chem. Lett.*, 2016, **7**, 4291–4296.
24 L. J. Hardwick, H. Buqa and P. Novák, *Solid State Ionics*, 2006, **177**, 2801–2806.
25 P. T. Barton, Y. D. Premchand, P. A. Chater, R. Seshadri and M. J. Rosseinsky, *Chem. – Eur. J.*, 2013, **19**, 14521–14531.
26 C. Ghanty, B. Markovsky, E. M. Erickson, M. Talianker, O. Haik, Y. Tal-Yossef, A. Mor, D. Aurbach, J. Lampert, A. Volkov, J.-Y. Shin, A. Garsuch, F. F. Chesneau and C. Erk, *ChemElectroChem*, 2015, **2**, 1479–1486.
27 C. Julien and M. Massot, *Solid State Ionics*, 2002, **148**, 53–59.
28 J. Molenda, P. Wilk and J. Marzec, *Solid State Ionics*, 2002, **146**, 73–79.
29 P. Vandenabeele, *Practical Raman Spectroscopy*, John Wiley & Sons, Incorporated, Belgium, 1st edn, 2013.
30 M. Bianchini, A. Schiele, S. Schweidler, S. Sicolo, F. Fauth, E. Suard, S. Indris, A. Mazilkin, P. Nagel, S. Schuppler, M. Merz, P. Hartmann, T. Brezesinski and J. Janek, *Chem. Mater.*, 2020, **32**, 9211–9227.
31 L. de Biasi, A. Schiele, M. Roca-Ayats, G. Garcia, T. Brezesinski, P. Hartmann and J. Janek, *ChemSusChem*, 2019, **12**, 2240–2250.
32 W. Li, J. N. Reimers and J. R. Dahn, *Solid State Ionics*, 1993, **67**, 123–130.

33 C. Xu, P. J. Reeves, Q. Jacquet and C. P. Grey, *Adv. Energy Mater.*, 2021, **11**, 1–12.
34 I. Konuma, N. Ikeda, B. D. L. Campéon, H. Fujimura, J. Kikkawa, H. D. Luong, Y. Tateyama, Y. Ugata, M. Yonemura, T. Ishigaki, T. Aida and N. Yabuuchi, *Energy Storage Mater.*, 2024, **66**, 103200.
35 M. E. Arroyo y de Dompablo, A. Van der Ven and G. Ceder, *Phys. Rev. B:Condens. Matter Mater. Phys.*, 2002, **66**, 1–9.
36 J. P. Peres, F. Weill and C. Delmas, *Solid State Ionics*, 1999, **116**, 19–27.
37 A. R. Genreith-Schriever, A. Alexiu, G. S. Phillips, C. S. Coates, L. A. V. Nagle-Cocco, J. D. Bocarsly, F. N. Sayed, S. E. Dutton and C. P. Grey, *Chem. Mater.*, 2024, **36**, 2289–2303.
38 S. Sicolo, M. Mock, M. Bianchini and K. Albe, *Chem. Mater.*, 2020, **32**, 10096–10103.